J Neurophysiol 122: 1036–1049, 2019.
First published July 10, 2019; doi:10.1152/jn.00326.2019.

RESEARCH ARTICLE | *Nervous System Pathophysiology*

Simulating perinodal changes observed in immune-mediated neuropathies: impact on conduction in a model of myelinated motor and sensory axons

Boudewijn T. H. M. Sleutjes,[1] Maria O. Kovalchuk,[1] Naric Durmus,[2,3] Jan R. Buitenweg,[2] Michel J. A. M. van Putten,[3,4] Leonard H. van den Berg,[1] and Hessel Franssen[1]

[1]*Department of Neurology, Brain Center Utrecht, University Medical Center Utrecht, Utrecht, The Netherlands;* [2]*Biomedical Signals and Systems, MIRA, Institute for Biomedical Technology and Technical Medicine, University of Twente, Enschede, The Netherlands;* [3]*Department of Clinical Neurophysiology, University of Twente, Enschede, The Netherlands; and* [4]*Department of Neurology and Clinical Neurophysiology, Medisch Spectrum Twente, Enschede, The Netherlands*

Submitted 22 May 2019; accepted in final form 7 July 2019

Sleutjes BT, Kovalchuk MO, Durmus N, Buitenweg JR, van Putten MJ, van den Berg LH, Franssen H. Simulating perinodal changes observed in immune-mediated neuropathies: impact on conduction in a model of myelinated motor and sensory axons. *J Neurophysiol* 122: 1036–1049, 2019. First published July 10, 2019; doi: 10.1152/jn.00326.2019.—Immune-mediated neuropathies affect myelinated axons, resulting in conduction slowing or block that may affect motor and sensory axons differently. The underlying mechanisms of these neuropathies are not well understood. Using a myelinated axon model, we studied the impact of perinodal changes on conduction. We extended a longitudinal axon model (41 nodes of Ranvier) with biophysical properties unique to human myelinated motor and sensory axons. We simulated effects of temperature and axonal diameter on conduction and strength-duration properties. We then studied effects of impaired nodal sodium channel conductance and paranodal myelin detachment by reducing periaxonal resistance, as well as their interaction, on conduction in the 9 middle nodes and enclosed paranodes. Finally, we assessed the impact of reducing the affected region (5 nodes) and adding nodal widening. Physiological motor and sensory conduction velocities and changes to axonal diameter and temperature were observed. The sensory axon had a longer strength-duration time constant. Reducing sodium channel conductance and paranodal periaxonal resistance induced progressive conduction slowing. In motor axons, conduction block occurred with a 4-fold drop in sodium channel conductance or a 7.7-fold drop in periaxonal resistance. In sensory axons, block arose with a 4.8-fold drop in sodium channel conductance or a 9-fold drop in periaxonal resistance. This indicated that motor axons are more vulnerable to developing block. A boundary of block emerged when the two mechanisms interacted. This boundary shifted in opposite directions for a smaller affected region and nodal widening. These differences may contribute to the predominance of motor deficits observed in some immune-mediated neuropathies.

NEW & NOTEWORTHY Immune-mediated neuropathies may affect myelinated motor and sensory axons differently. By the development of a computational model, we quantitatively studied the impact of perinodal changes on conduction in motor and sensory axons. Simulations of increasing nodal sodium channel dysfunction and paranodal myelin detachment induced progressive conduction slowing. Sensory axons were more resistant to block than motor axons. This could explain the greater predisposition of motor axons to functional deficits observed in some immune-mediated neuropathies.

computational model; conduction slowing and block; myelinated motor and sensory axon; nodal sodium channel disruption; paranodal myelin detachment

INTRODUCTION

Immune-mediated polyneuropathies may affect myelinated nerve fibers, including the myelin sheath, the node of Ranvier, the adhesion molecules binding the axonal membrane to the Schwann cell membrane, and the axonal membrane itself (Kieseier et al. 2018). These neuropathies include the acute inflammatory demyelinating polyneuropathy (AIDP) and acute motor axonal neuropathy (AMAN) variants of the Guillain-Barré syndrome, chronic inflammatory demyelinating polyneuropathy (CIDP), multifocal motor neuropathy (MMN), and anti-myelin-associated (anti-MAG) glycoprotein neuropathy. Developing disease-specific treatments poses a significant challenge because the selective vulnerability of motor or sensory nerve fibers and corresponding downstream mechanisms have not been fully elucidated. Because the primary function of myelinated nerve fibers involves efficient transmission of action potentials, their damage will eventually present clinically by loss of muscle strength, loss of sensation, or both. A better understanding of the key mechanisms that hamper impulse transmission via saltatory conduction may potentially help to develop more targeted treatments aimed at prevention of irreversible nerve damage.

Studying the underlying pathology in patients with standard nerve conduction studies may not always provide sufficient detail because conduction slowing and block may originate from the malfunctioning of a variety of components in myelinated nerve fibers (Burke et al. 2001; Franssen 2015). Nerve excitability testing is an attractive translational method in which threshold changes, induced by various conditioning stimuli, can be ascribed to changes in ion channel activity at one site of a group of axons. However, detailed aspects of the relation between pathological and heterogeneous pathophysiological disease processes at single-axon level cannot be ade-

Address for reprint requests and other correspondence: B. T. H. M. Sleutjes, Dept. of Neurology, F02.230, University Medical Center Utrecht, PO Box 85500, 3508 GA Utrecht, The Netherlands (e-mail: b.sleutjes@umcutrecht.nl).

Table 1. *Overview of morphological and electrical parameters of model*

	Morphological Parameters	
Nerve fiber	Diameter	10 μm
Node to node	Distance	1,150 μm
Node	Length	1 μm
	Diameter	3.3 μm
Paranode	Length, per segment	3 μm
	Diameter	3.3 μm
	Periaxonal space width	0.004 μm
Juxtaparanode	Length, per segment	46 μm
	Diameter	6.9 μm
	Periaxonal space width	0.004 μm
Standard internode	Length, per segment	175.2 μm
	Diameter	6.9 μm
	Periaxonal space width	0.004 μm
Myelin	Capacitance	0.1 μF/cm^2
	Conductance	0.001 S/cm^2
	No. of myelin lamella	120
Longitudinal resistivity	Axoplasmatic	70 Ω·cm
	Periaxonal	70 Ω·cm

Parameters were obtained from McIntyre et al. (2002).

quately assessed in ex vivo models such as voltage-clamp experiments (Franssen and Straver 2014). Animal models that accurately mimic human pathology specifically in motor and sensory axons are available for AMAN (Yuki et al. 2001) and to a limited extent for AIDP, but not for CIDP and MMN. Studies of computational models of myelinated axons have emerged to provide a quantitative view of the vital mechanisms for adequate saltatory conduction (Blight 1985; Fitzhugh 1962; Goldman and Albus 1968; Halter and Clark 1991; Koles and Rasminsky 1972; McIntyre et al. 2002; Moore et al. 1978; Smit et al. 2009; Stephanova and Bostock 1995). By systematically investigating pathological processes that cannot be examined otherwise, they may assist in defining avenues for developing disease-specific treatments.

Emerging insights into the pathology of immune-mediated neuropathies have shown specific targeting of molecular complexes that characterize the distinct geometrical domains surrounding the node of Ranvier, including the paranode and juxtaparanode (Delmont et al. 2017; Devaux et al. 2016; Susuki 2013; Uncini and Kuwabara 2015). Physiologically, these perinodal domains also have a vital role in saltatory conduction and recovery following action potentials (Barrett and Barrett 1982; Halter and Clark 1991; McIntyre et al. 2002). Moreover, biophysical differences between motor and sensory axons have often been proposed as potentially contributing to the varied degree of functional impairment in immune-mediated neuropathies (Burke et al. 2017). However, the interplay of these biophysical differences and the pathological processes related to immune-mediated neuropathies with the occurrence of conduction block remains yet unclear. This emphasizes the need for a computational model with a sufficient geometrical and biophysical description to systematically study pathological processes and their impact on conduction in motor and sensory axons.

Our study presents an extended longitudinal myelinated axon model, modified from McIntyre et al. (2002) by including axonal ion channel properties under the myelin sheath, based on experimental mammalian (Waxman et al. 1995) and human nerve excitability studies (Howells et al. 2012; Jankelowitz et al. 2007; Kiernan et al. 2005). Our model allows biophysical characteristics unique to human myelinated motor and sensory axons to be implemented (Berthold and Rydmark 1995; Bostock et al. 1994; Bostock and Rothwell 1997; Howells et al. 2012; Kiernan et al. 2004; Mogyoros et al. 1996, 1997; Ritchie 1995; Schwarz and Eikhof 1987; Schwarz et al. 1995). We simulated various physiological conditions and have shown that these are in agreement with experimental studies. In addition, we explored how saltatory conduction will be affected by some putative mechanisms associated with immune-mediated neuropathies, focusing on loss of functioning nodal sodium channels and disruption of the surrounding paranodal seal (Susuki 2013; Uncini and Kuwabara 2015).

METHODS

Model structure and anatomical properties of the myelinated axon model. We applied the double cable structure described by McIntyre et al. (2002). As a starting point, we used the MATLAB implementation of this model as published by Danner and colleagues (Danner et al. 2011a, 2011b; Krouchev et al. 2014). The model accurately describes the anatomy of a myelinated axon where a successive node-internode configuration consists of a node (1 segment), paranode (1 segment), juxtaparanode (1 segment), standard internode (6 segments), and again, a juxtaparanode (1 segment) and paranode (1 segment). Except for the nodal segments, the nonnodal (paranode, juxtaparanode, and standard intermode) segments are surrounded by a myelin sheath in which the periaxonal space was connected to the extracellular space by a myelin capacitance and conductance. Using Kirchoff's first law, each segment k was coupled with the previous segment ($k - 1$) and next segment ($k + 1$), where the nonnodal

Table 2. *Maximum conductances, specific capacitances, and resting membrane potential of motor and sensory axon model*

Parameter	Abbreviation	Motor	Sensory[a]
Node			
Transient sodium conductance, S/cm^2	g_{Na_t}	3.0	
Persistent sodium conductance, S/cm^2	g_{Na_p}	0.01	
Slow potassium conductance, S/cm^2	g_{K_s}	0.08	0.064
Leak conductance, S/cm^2	g_{L_k}	0.007	
Nodal capacitance, μF/cm^2	C_{node}	2	
Paranode			
Paranodal capacitance, μF/cm^2	C_p	2	
Paranodal conductance, S/cm^2	g_p	0.001	
Juxtaparanode			
Juxtaparanodal capacitance, μF/cm^2	C_{jp}	2	
Juxtaparanodal conductance, S/cm^2	g_{jp}	0.0001	
Fast potassium conductance, S/cm^2	g_{Kf}	0.02	
Standard internode			
Sodium conductance, S/cm^{2c}	g_{Nat}	0.03	
Slow potassium conductance, S/cm^{2c}	g_{Ks}	0.0027	0.0022
Fast potassium conductance, S/cm^{2c}	g_{Kf}	0.0033	
Leak conductance, S/cm^2	g_{Lk}	0.0001	
HCN conductance, S/cm^{2d}	g_{HCN}	0.0014	
Electrogenic pump current, pA[e]	I_{pump}	100	
Internodal capacitance, μF/cm^2	C_i	2	
Resting membrane potential, mV[b]	V_{rest}	−84.9	−81.8

Unless indicated, parameters were obtained from McIntyre et al. (2002). Absolute values were calculated using diameter and length of the regions (Table 1) by assuming circular symmetry. [a]Biophysical differences between motor and sensory axons (see text and APPENDIX). [b]Resting membrane potentials achieved with the new models (see text). [c]Internodal conductances relative to nodal conductances (see text). [d]Determined to satisfy internodal ionic equilibrium at resting membrane potential. [e]Pump current similar to that previously applied (Stephanova and Bostock 1995).HCN, hyperpolarizing-activated nucleotide-gated cation channel.

segments required calculation of the potential across the inner-axonal/periaxonal and periaxonal/extracelullar space. Because the nodal segment did not involve the periaxonal space, it included the potential across inner-axonal/extracellular space, which equals the nodal membrane potential (Danner et al. 2011b). For the longitudinal model, we used a total of 41 nodes of Ranvier separated by 40 internodes. The membrane potential was clamped at its resting membrane potential. Table 1 gives a detailed summary of the morphological and electrical parameters of these segments (McIntyre et al. 2002) based on microscopic-anatomical mammalian studies (Waxman et al. 1995).

Motor axon: nodal, juxtaparanodal, and internodal ion channel conductances. Similar to the original model (McIntyre et al. 2002), the node of Ranvier consists of voltage-gated transient and persistent sodium channels, voltage-gated slow potassium channels, a leak channel, and nodal membrane capacitance. Their conductances are given in Table 2 and the gating kinetics in the APPENDIX.

To accurately simulate internodal membrane dynamics, the original passive description was modified by implementing juxtaparanodal and internodal voltage-gated fast potassium channels and internodal voltage-gated sodium, slow potassium, and hyperpolarizing-activated nucleotide-gated cation (HCN) channels. Density of nodal sodium channels is significantly higher (1,000–2,000 channels/μm^2) than at the internode (<25 channels/μm^2) (Waxman et al. 1995). By taking a physiological ratio of 100 (2,000 channels/μm^2 divided by 20 channels/μm^2), the internodal sodium conductance was set at $^1/_{100}$ of the nodal sodium conductance. To reduce complexity, internodal sodium channels in a persistent state were omitted. Because the density of internodal slow potassium channels was suggested to be approximately $^1/_{30}$ of their nodal density, the internodal-to-nodal conductance ratio was set at $^1/_{30}$ (Waxman and Ritchie 1993). Based on the same study, internodal fast potassium conductance was set at $^1/_6$ of juxtaparanodal conductance (Waxman and Ritchie 1993). The location of Na^+-K^+ pumps is still ambiguous. Early work suggested a nodal location, but subsequent electrophysiological and staining experiments suggested an internodal location (Kleinberg et al. 2007; Waxman et al. 1995). Therefore, an electrogenic pump current was implemented in the internode. Based on the above modifications, a conductance for HCN channels was applied to satisfy internodal ionic equilibrium at the resting membrane potential, which was set at −84.9 mV (see Table 2 and APPENDIX). A schematic view of the new model is shown in Fig. 1.

Sensory axon: biophysical differences with respect to motor axon. Sensory axons were suggested to have greater inward rectifying current (Bostock et al. 1994). Responses to long-lasting hyperpolarization revealed that a major part of this greater current originates from changes in gating kinetics of HCN channels, which was best modeled by depolarizing their half-activation potential (Howells et al. 2012). In our model, this half-activation was depolarized by 6.3 mV. Furthermore, a reduced slow potassium channel expression was hypothesized to contribute to the increased susceptibility of ectopic activity in sensory axons (Baker et al. 1987; Howells et al. 2012; Kocsis et al. 1987). This was modeled by reducing the slow potassium conductance in the sensory axon model by 20% relative to the motor axon. Subsequently, broadening of the sensory action potential due to a reduction in slow potassium channel was compensated by accelerating the activation gate and slowing the inactivation gate of sensory sodium channels (Honmou et al. 1994; Howells et al. 2012; McIntyre et al. 2002; Mitrović et al. 1993; Schwarz et al. 1983) (see APPENDIX). With these biophysical differences, an ionic equilibrium was achieved when sensory resting membrane potential was set at −81.8 mV (see Table 2 and APPENDIX). Without altering the amount of sodium channels in persistent state, the depolarized membrane potential of 3.1 mV in sensory axons (motor vs. sensory: −84.9 vs. −81.8 mV) approximately doubled the persistent sodium current at resting membrane potential, which was also suggested to be an important biophysical difference (Bostock and Rothwell 1997; Howells et al. 2012).

Simulation and stimulation settings. Numerical integration of the differential equations was performed within MATLAB (R2014b; The MathWorks, Natick, MA) using the SUNDIALS CVode package (version 2.6.1; Hindmarsh et al. 2005) with time steps of 10 μs. To

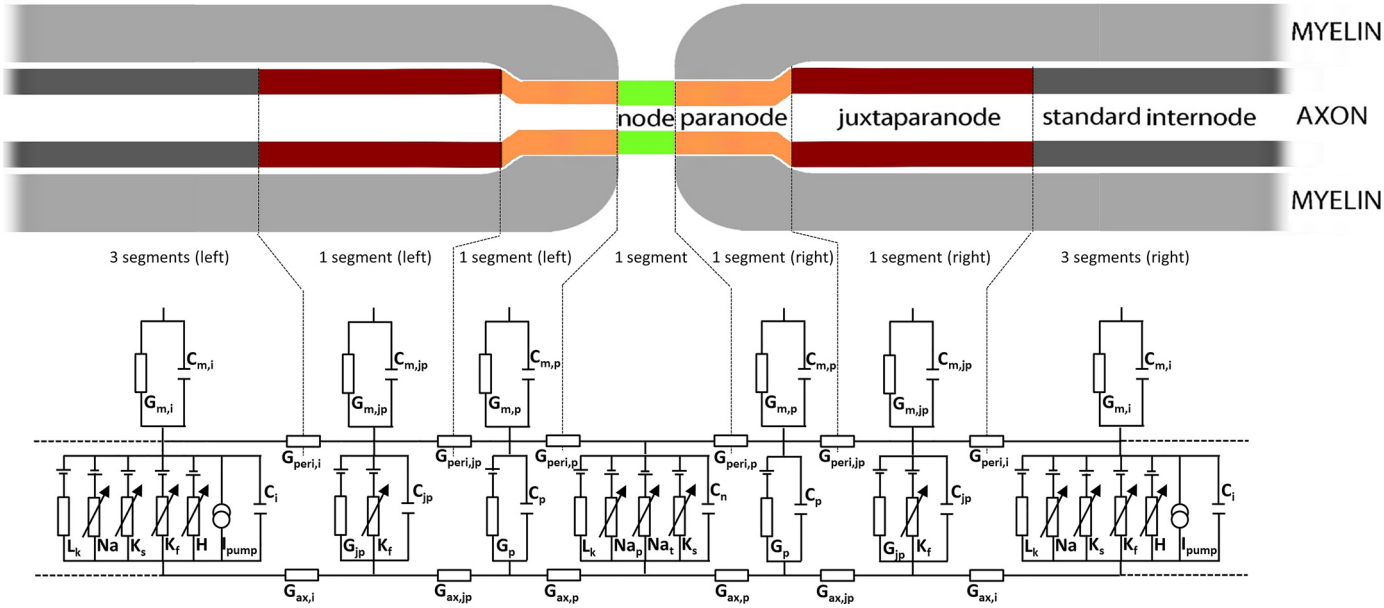

Fig. 1. The longitudinal myelinated axon model. A schematic view of a myelinated axon [modified from Franssen and Straver (2013) with permission from Wiley Periodicals, Inc.] with an electric circuit diagram of the new model showing the nodal, paranodal, juxtaparanodal, and internodal regions. The nodal domain (1 segment) contains persistent (Na_p) and transient sodium (Na_t) channels, slow potassium (K_s) and leak (L_k) channels, and the nodal capacitance (C_n) in the axonal membrane. The paranodal domain (2 segments, 1 left and 1 right) contains, in the axonal membrane, a linear conductance with, in parallel, a capacitance (G_p and C_p). The juxtaparanodal domain (2 segments, 1 left and 1 right) contains, in the axonal membrane, fast potassium channels (K_f) and, in parallel, a linear conductance (G_{jp}) and capacitance (C_{jp}). The internodal domain (6 segments, 3 left and 3 right) contains sodium channels (Na), fast (K_f) and slow (K_s) potassium channels, a leak (L_k) conductance, I_h-channels (H), an electrogenic pump (I_{pump}), and an internodal capacitance (C_i) in the axonal membrane. The myelin sheath is represented by a linear conductance with, in parallel, a capacitance in the paranode ($G_{m,p}$ and $C_{m,p}$), juxtaparanode ($G_{m,jp}$ and $C_{m,jp}$), and internode ($G_{m,i}$ and $C_{m,i}$) (see Table 2). Longitudinally, the model contains axonal (G_{ax}) and periaxonal (G_{peri}) resistivities (see Table 2).

calculate the conduction velocity, first, the derivative of the membrane potential was taken in every node, and from this the time points with maximum gradient were determined. To provide an estimate of conduction velocity, the distance between *nodes 11* and *31* was divided by the time interval with maximum gradient at these nodes. The nodal excitation threshold and severity levels of pathological conditions that blocked saltatory conduction were determined using a binary search algorithm based on Hennings et al. (2005). These severity levels, expressed as a percentage of normal, were determined with a binary search stop criteria of 0.5% and subsequently rounded down to the integer that induced a block. Similarly to a previous study (Hales et al. 2004), when the membrane potential reached a target level (0 mV in our simulations), a generated action potential was detected. To avoid boundary effects of the model, results of the simulations were derived from the middle nodes (*nodes 11–31*). Single intracellular stimuli were delivered with a stimulus duration of 1 ms and a fixed stimulus intensity set at three times the excitation threshold at *node 11*.

Simulating effects of temperature, axon diameter, and strength-duration properties. The relation between conduction velocity and myelinated axon diameter was simulated by increasing axon diameter from 10 μm (default) to 14 and 16 μm. In conjunction, other parameters were also scaled (see Table 1 in McIntyre et al. 2002), including the nodal (3.3, 4.7, and 5.5 μm), paranodal (3.3, 4.7, and 5.5 μm), juxtaparanodal (6.9, 10.4, and 12.7 μm), standard internodal diameter (6.9, 10.4, and 12.7 μm), node-to-node distance (1,150, 1,400, and 1,500), and number of myelin lamellae (120, 140, and 150). The effect of temperature on conduction velocity was modeled by varying temperature from 30°C to 36°C (default temperature) in steps of 2°C. Rheobase and strength-duration time constant were determined by using Weiss's law (Bostock 1983; Mogyoros et al. 1996) and assessing excitation thresholds at five different stimulus durations (1, 0.8, 0.6, 0.4, and 0.2 ms) at the middle node (*node 21*).

Simulating nodal sodium channel disruption and loss of paranodal seal. Several mechanisms in immune-mediated neuropathies have been suggested in which the node of Ranvier and its surrounding structures play an important role (Kieseier et al. 2018). For instance, in MMN, half of the patients have high titers of serum antibodies against ganglioside GM1, which is expressed on the axolemma of the nodes of Ranvier and perinodal Schwann cells. Ganglioside GM1 was suggested to contribute to nodal sodium channel clustering and paranodal stabilization (Susuki et al. 2007a, 2007b, 2012). Disrupted sodium channel clustering and paranodal myelin detachment at both sides of the nodes may contribute to the development of conduction slowing and eventually block. Simulations were performed to quantify how these mechanisms affect saltatory conduction. Disrupted sodium channel clustering may result in decreased inward sodium current density (reviewed by Kaji 2003). In the present study, this was simulated by decreasing maximum transient and persistent sodium channel conductances (Fig. 1; nodal Na_p and Na_t). Broken paranodal seals were simulated by decreasing the periaxonal resistance across the paranodal region such that juxtaparanodal fast potassium channels also become exposed to the extracellular medium (Fig. 1; increasing the periaxonal paranodal conductance $G_{peri,p}$ and the juxtaparanodal conductance $G_{peri,jp}$).The resulting effective increase in nodal area was simulated by increasing nodal capacitance (Fig. 1; C_n). The affected region involved the nine middle nodes (*nodes 17–25*) and the paranodal structures between them.

RESULTS

Validation of motor and sensory axon model. Figure 2 illustrates an action potential in a myelinated motor and a myelinated sensory axon obtained at the middle node (*node 21*) after application of a single pulse at *node 11*. The excitation thresholds at *node 11* were 577 pA for the motor axon and 403 pA for the sensory axon. The action potential was followed by the physiologically characteristic depolarizing afterpotential (DAP) and hyperpolarizing afterpotential (HAP) (*inset* in Fig. 2*A*). Action potential duration (halfway resting and peak potential) was longer for the motor axon (0.34 ms) than for the sensory axon (0.29 ms). With a modeled diameter of 10 μm, the action potential propagation (*nodes 11–31*) was in the physiological range with a conduction velocity of 47.9 m/s for the motor axon (Fig. 3) and 50.0 m/s for the sensory axon (Boyd and Kalu 1979).

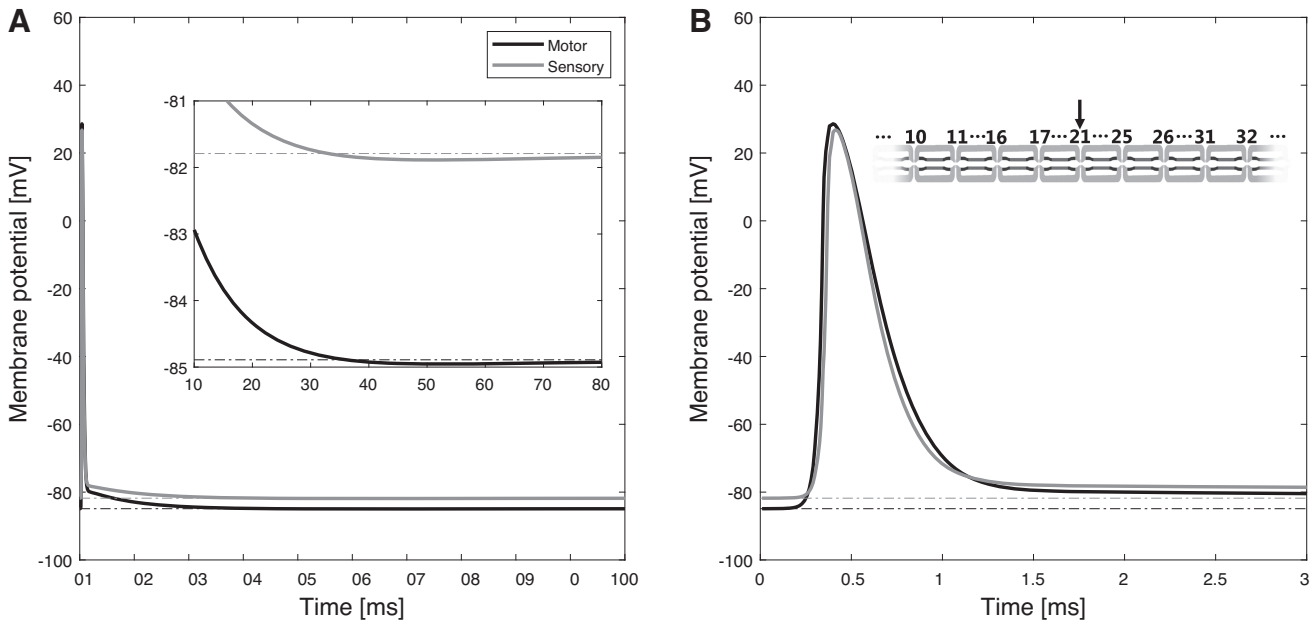

Fig. 2. Motor and sensory action potential generation. *A* and *B*: generated action potential for the motor (black) and sensory (gray) myelinated axon up to 100 ms (*A*) and up to 3 ms (*B*) at *node 21* after a 1-ms intracellular stimulus pulse of 3 times the excitation threshold at *node 11*. In *A*, *inset*, the action potential close to the resting membrane potential is also shown. Dotted lines represent resting membrane potential.

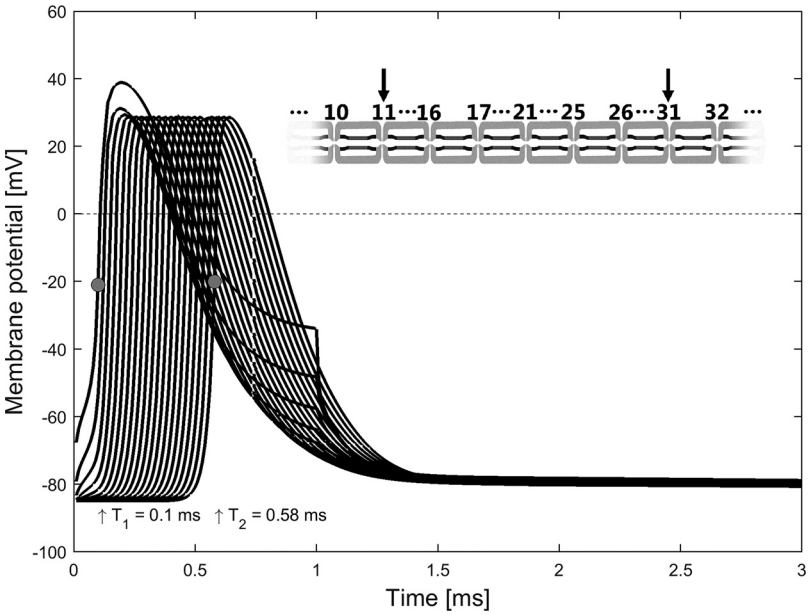

Fig. 3. Motor action potential propagation. Action potential propagation of the motor myelinated axon model up to 3 ms from *node 11* to *node 31*. The dots at *node 11* ($T_1 = 0.10$ ms) and 31 ($T_2 = 0.58$ ms) define the time points with the highest gradient of membrane potential from which the conduction velocity was derived [$(20 \times 1{,}150\ \mu m)/(T_2 - T_1) = 47.9$ m/s].

Conduction velocity increased approximately linearly with axon diameter to 70.0 m/s (14 μm) and 83.3 m/s (16 μm) in motor axons and to 73.7 m/s (14 μm) and 88.2 m/s (16 μm) in sensory axons (Fig. 4*A*). Conduction velocities also increased linearly with temperature (Fig. 4*B*), the increase being 1.60 $m \cdot s^{-1} \cdot °C^{-1}$ for the motor and 1.58 $m \cdot s^{-1} \cdot °C^{-1}$ for the sensory axon. After conversion to Q_{10} with the conduction velocities at 30°C and 36°C, Q_{10} was 1.45 for the motor axon and 1.43 for the sensory axon, thereby falling within the range of physiologically observed temperature dependence (Davis et al. 1976; Lowitzsch et al. 1977; Paintal 1965; Rasminsky 1973).

Figure 5 illustrates the strength-duration properties for motor and sensory axons determined at the middle node. It must be emphasized that simulations with intracellular stimulation result in a shorter strength-duration time constant (SDTC) compared with experiments with transcutaneous stimulation due to the large nerve/electrode distance (Kuhn et al. 2009). The motor rheobase was 476 pA and the motor SDTC was 205 μs, which closely match values in previous modeling studies (Bostock 1983; Daskalova and Stephanova 2001; McIntyre et al. 2002). In agreement with experimental studies, the SDTC in the sensory axon (304 μs) was higher and the rheobase was lower (308 pA) compared with values in the motor axon. This results in a ratio of 1.5 for sensory/motor SDTC (304/205 μs), which matches with experimental observations (Kovalchuk et al. 2018; Mogyoros et al. 1996).

Disruption of nodal sodium channel clusters in motor and sensory axon. Figure 6A shows motor action potential propagation from *node 11* to *node 31* for a 70% of normal nodal sodium channel conductance. A small drop in the maximal membrane potential can be observed at the affected middle nodes with a slowed conduction velocity to 43.4 m/s. Failure of motor action potential propagation occurred at a nodal sodium channel conductance of 25% of normal (4-fold drop; Fig. 6*B*). To determine the effect of disruption of nodal sodium channel clusters on motor and sensory conduction velocities, nodal sodium channel conductance was reduced from 100% (normal), 70%, 50%, and 30% up to conduction block. In sensory axons, action potential propagation failure occurred at a conductance of 21% of normal (4.8-fold drop). Decreasing nodal sodium channel conductance induced progressive slowing toward block in the motor and sensory axons, with slightly higher conduction velocities and more resistance to conduction block for the sensory axon (Fig. 7).

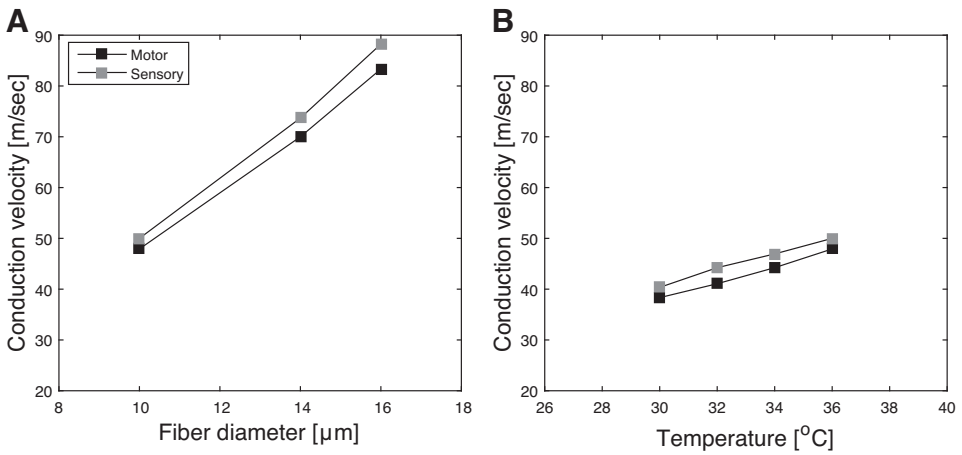

Fig. 4. Effect of axon diameter and temperature on conduction velocity. *A*: effect of increase in myelinated fiber diameter of motor (black) and sensory (gray) myelinated axons on conduction velocity. *B*: relation between temperature and conduction velocity for the motor (black) and sensory (gray) myelinated axons.

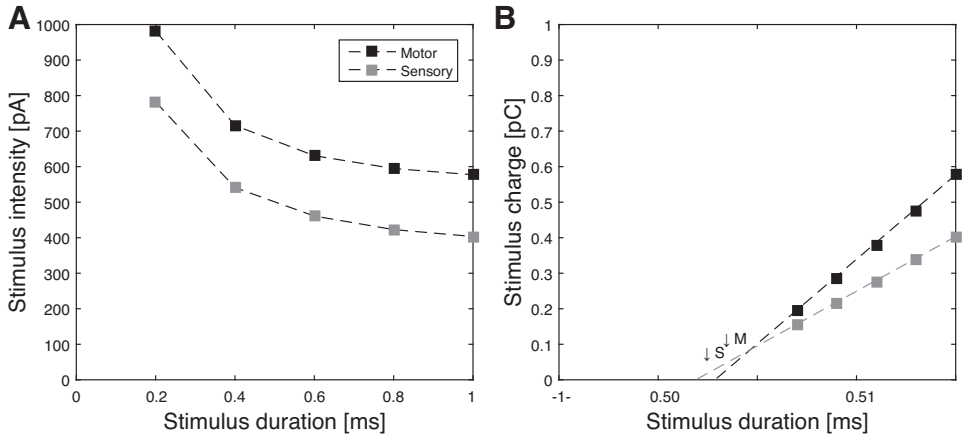

Fig. 5. Motor and sensory strength-duration properties. *A*: stimulus duration curve for motor (black) and sensory (gray) myelinated axons. *B*: same result as in *A*, but after conversion to the charge-duration curve. Vertical arrows indicate the cross sections with the *x*-axis, which correspond with the strength-duration time constant (M, motor = 205 μs; S, sensory = 304 μs).

Paranodal myelin loop detachment in motor and sensory axon. Detachment of paranodal myelin loops from the axonal membrane in motor and sensory axons was simulated by decreasing the periaxonal resistance to 70%, 50%, 30%, and 20% of normal. Motor conduction velocity decreased to 44.2 (70% of normal), 41.1 (50% of normal), 35.4 (30% of normal; Fig. 8*A*) and 28.0 m/s (20% of normal) until conduction block occurred at a periaxonal resistance of 13% of normal (Fig. 8*B*).

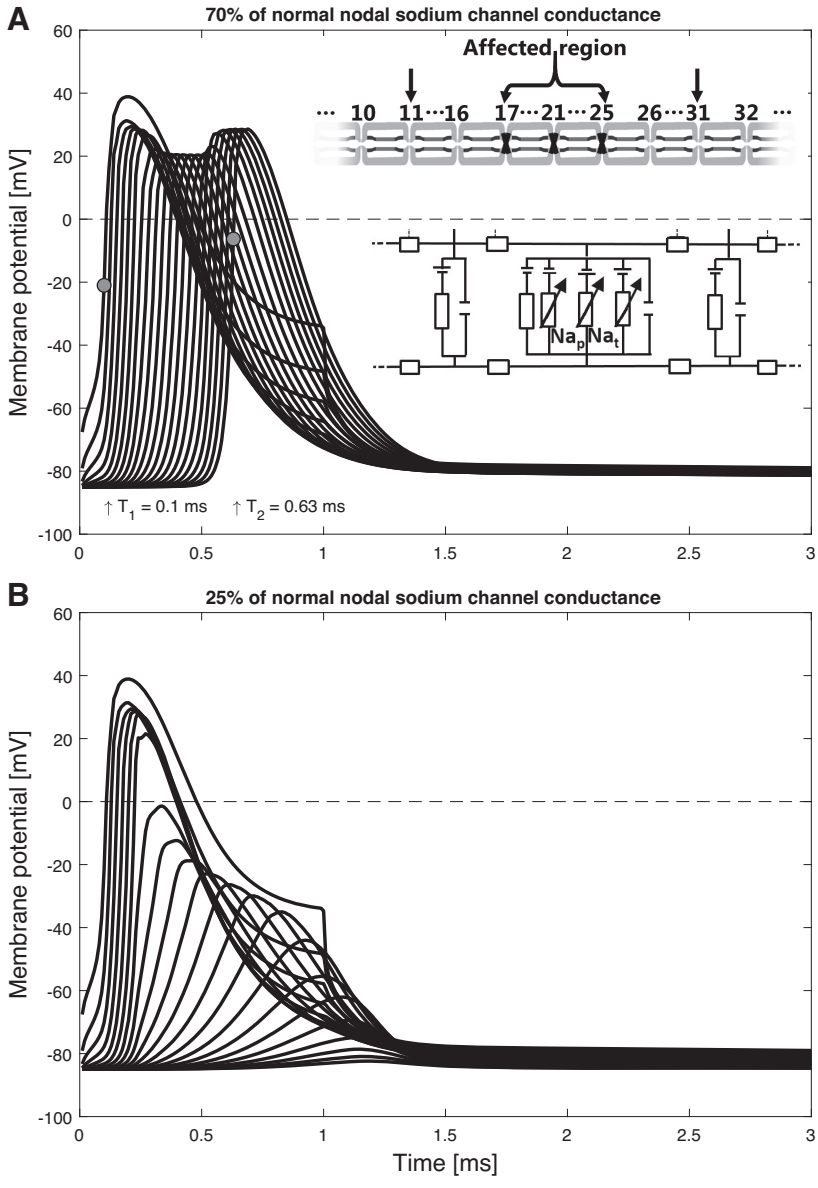

Fig. 6. Motor action potential slowing and conduction block due to disrupted nodal sodium channel clusters. Action potential propagation of the motor myelinated axon model up to 3 ms from *nodes 11* to *31*, with 70% of normal nodal sodium channel conductance (*A*) resulting in a slight drop of the maximum membrane potential around the affected region and conduction slowing [(20 × 1,150 μm)/($T_2 - T_1$) = 43.4 m/s], and 25% of normal nodal sodium channel conductance (*B*) inducing a conduction block for stimulation at *node 11* at 3 times the excitation threshold. *Insets* in *A* show a schematic view of the myelinated axon with the affected region (*top*) and the characteristics of the myelinated axon being modeled (*bottom*), the persistent (Na_p) and transient (Na_t) sodium channel conductances.

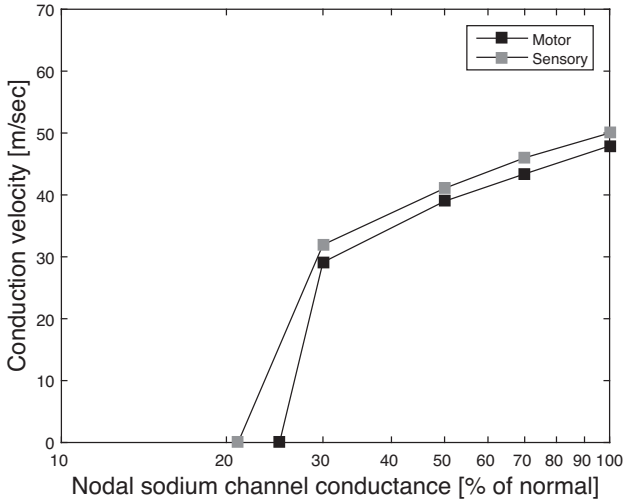

Fig. 7. Relation of motor and sensory conduction slowing toward block with increasing nodal sodium channel cluster disruption. Relation between nodal sodium channel cluster disruption is simulated by decreasing the sodium channel conductance from 100% (normal), 70%, 50%, and 30% and decreasing conduction velocities in motor (black) and sensory (gray) axons until conduction block (motor = 25% of normal; sensory = 21% of normal). Note the logarithmic scaling of the *x*-axis.

Sensory conduction velocity decreased to 46.9 (70% of normal), 44.2 (50% of normal), 37.7 (30% of normal), and 30.7 m/s (20% of normal) until conduction block occurred at a periaxonal resistance of 11% of normal (9-fold drop). Decreasing periaxonal resistance induced progressive slowing toward block in the motor and sensory axons, where the sensory axon had slightly faster conduction velocities and was more resistant to conduction block (Fig. 9).

Interaction of disrupted nodal sodium channel clusters and paranodal myelin loop detachment. More sophisticated simulations were subsequently performed to the interaction of nodal sodium channel disruption and detachment of paranodal myelin loops on conduction slowing and block. Figure 10*A* shows that a boundary of block emerges, representing the percentage of normal where this interaction induces conduction block. Outside this boundary (Fig. 10*A*, *bottom left*), there is failure of saltatory conduction, and within this boundary (Fig. 10*A*, *top right*), saltatory conduction is still maintained, albeit at lower conduction velocities. The sensory axon, compared with the motor axon, had consistently higher resistance to the emergence of block. Finally, for the motor axon, we completely mapped the conduction velocity distribution within the boundary of block in two-dimensional (Fig. 10*B*, *top*) and projected three-dimensional representations (Fig. 10*B*, *bottom*), which also encompass the results of Figs. 7 and 9.

Sensitivity of the boundary of block to enlarged nodal area. Depending on various pathophysiological conditions and their severity levels, the boundary of block shifts, changing the areas covered by conduction slowing and block. To investigate the sensitivity of this boundary, two additional conditions were simulated in the motor axon. Because damage may appear more focally, the affected region was reduced to five nodes (*nodes 19–23*). Also, paranodal myelin detachment may, as an additional consequence, effectively enlarge the exposed nodal area. An enlarged nodal area was simulated by increasing the nodal capacitance that reflects widening of nodal length from 1 to 3 μm. Figure 10*C* shows that the two conditions shift the boundary of block in opposite directions. When only five nodes are affected, the area covered by conduction block is reduced, whereas for nodal widening this area increases.

DISCUSSION

In this study we successfully implemented a mathematical model to simulate saltatory conduction along peripheral myelinated motor and sensory axons in circumstances resembling those hypothesized in immune-mediated neuropathies. The simulations with the model generated action potentials followed by the physiological depolarizing and hyperpolarizing afterpotentials. Our model further corresponded with experimental and simulation studies on motor and sensory conduction velocities that scaled linearly with temperature and axonal diameter (Boyd and Kalu 1979; Davis et al. 1976; de Jesus et al. 1973; Franssen and Wieneke 1994; Lowitzsch et al. 1977). Also, the motor and sensory strength-duration properties followed the behavior observed in human peripheral myelinated nerves (Howells et al. 2013; Kiernan et al. 2000, 2001; Kovalchuk et al. 2018; Mogyoros et al. 1996; Sleutjes et al. 2018) Subsequently, we were able to quantitatively determine that saltatory conduction progressively slows before conduction block when pathology associated with immune-mediated neuropathies was induced, by focusing on disrupted nodal sodium channel clusters and paranodal detachment (Franssen and Straver 2014; Kieseier et al. 2018; Susuki et al. 2012; Uncini and Kuwabara 2015). A boundary of block emerged when the interaction of both mechanisms was simulated, with block occurring outside this boundary and slowing when remaining within this boundary. Simulations provided a link between the biophysical differences characteristic for motor and sensory axons and their varied impact on the emergence of conduction block. This provides quantitative evidence of their differential susceptibility to conduction block (Burke et al. 2017), which may also consequently induce a varied degree of functional impairment.

Differences between motor and sensory fibers. The implemented biophysical differences between motor and sensory axons are based on experimental evidence and simulations obtained from human nerve excitability studies (Bostock et al. 1994; Bostock and Rothwell 1997; Howells et al. 2012). With the use of these differences, our findings support the studies suggesting that sodium gating kinetics may underlie the narrower sensory action potential compared with motor action potential (Burke et al. 1997; Howells et al. 2012; McIntyre et al. 2002), despite the larger persistent sodium current and smaller slow potassium conductance in normal sensory compared with motor axons. Sensory conduction velocity was also previously found to be slightly higher than the motor nerve conduction velocity (Nielsen 1973). The slopes of the conduction velocity due to temperature changes (1.6 $m \cdot s^{-1} \cdot °C^{-1}$) were approximately linear and fell within the experimentally observed ranges for motor and sensory axons (1.1–2.3 $m \cdot s^{-1} \cdot °C^{-1}$) (Davis et al. 1976; de Jesus et al. 1973; Franssen and Wieneke 1994; Halar et al. 1980; Lowitzsch et al. 1977; Rasminsky 1973). Modeled strength-duration properties were in agreement with previous modeled values (Bostock 1983; Daskalova and Stephanova 2001; McIntyre et al. 2002). Single intracellular stimuli applied at a node results in shorter simu-

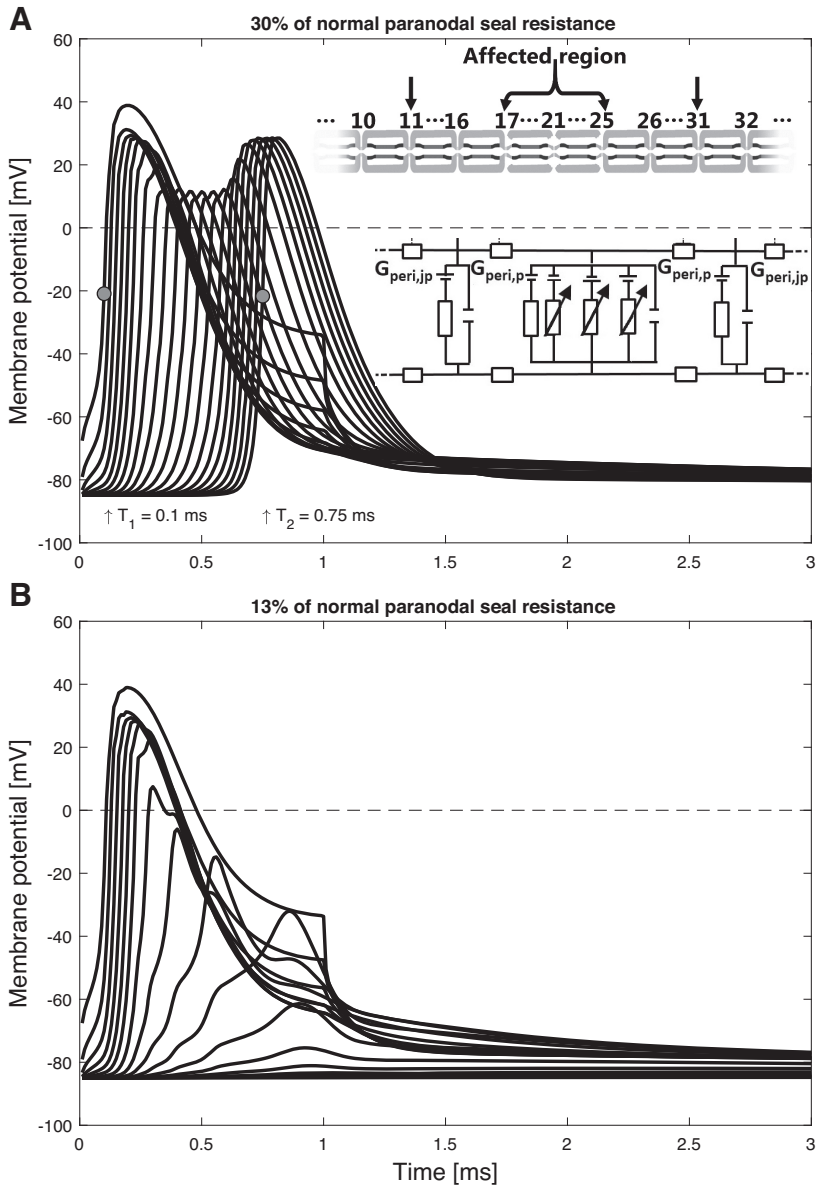

Fig. 8. Motor action potential slowing and conduction block due to paranodal myelin loop detachment. Action potential propagation of the motor myelinated axon model up to 3 ms from *nodes 11* to *31* with 30% of normal paranodal seal resistance (*A*) resulting in a slight drop of the maximum membrane potential around the affected region and conduction slowing [$(20 \times 1{,}150\ \mu m)/(T_2 - T_1) = 35.4$ m/s] and 13% of normal paranodal seal resistance (*B*) inducing a conduction block for stimulation at *node 11* at 3 times the excitation threshold. *Insets* in *A* show a schematic view of the myelinated axon with the affected region (*top*) and the characteristics of the myelinated axon being modeled (*bottom*), the periaxonal paranodal ($G_{peri,p}$) and juxtaparanodal conductance ($G_{peri,jp}$).

lated SDTC compared with experiments with large nerve/electrode distance (Kuhn et al. 2009). Uniform stimulation over all nodes and internodes has been suggested to more closely approximate external stimulation with large surface electrodes (Daskalova and Stephanova 2001). It should be further noted that studying single axons (Mogyoros et al. 1996; Sleutjes et al. 2018) results in a larger physiological range for strength-duration properties compared with assessing a group of axons. The sensory-to-motor SDTC ratio of 1.5 (304/205 μs) was also in accordance with previous studies (Howells et al. 2012; Kiernan et al. 2000, 2001; Kovalchuk et al. 2018; Mogyoros et al. 1996). Although the excitation threshold depends on many factors, the order of magnitude (≈0.1–1 nA) to generate an action potential resembled that of other modeling results (Bostock 1983; Danner et al. 2011b; Stephanova and Bostock 1995). With the implemented biophysical differences between motor and sensory axons, our simulations showed that they responded differently to conduction slowing and emergence of block induced by nodal and paranodal dysfunction at various severity levels. Differences in motor and sensory axons are likely not limited to axonal membrane dynamics, but might also include microstructural components. This may further contribute to the varied susceptibility and selectivity of motor and sensory involvement in immune-mediated neuropathies. Although more difficult to elucidate, adequate implementation of these differences may further improve computational models to study immune-mediated neuropathies more specifically.

Emergence of conduction block. Inducing conduction block required considerable blockage of sodium channels (4- to 5-fold) and reduction of the paranodal seal resistance (8- to 9-fold), emphasizing that the safety factor for impulse generation is generally high. Normal axons have a safety factor, defined as the ratio of available to required driving current to excite a node, in the same order of magnitude (~5–7; Tasaki 1953). Our simulations further suggest that the smaller the area (Fig. 10*B*, *top*) or volume (Fig. 10*B*, *bottom*) in the multidimensional diagrams covered by conduction slowing relative to

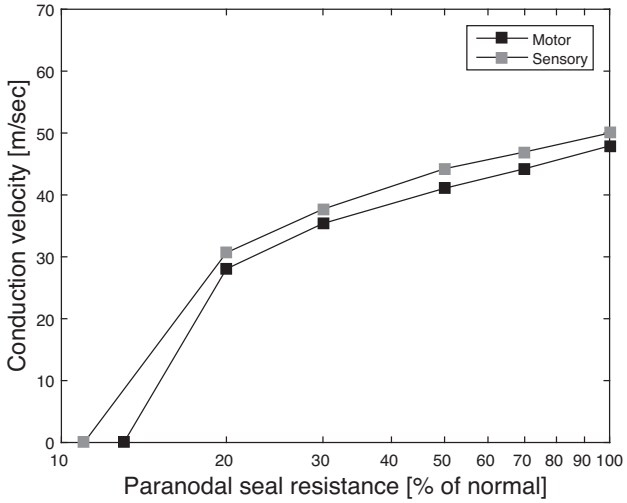

Fig. 9. Relation of motor and sensory conduction slowing toward block with increasing detachment of paranodal myelin loops. Relation between detachment of paranodal myelin loops is simulated by decreasing the paranodal seal resistance from 100% (normal), 70%, 50%, 30%, and 20% of normal and the decreasing conduction velocities in motor (black) and sensory (gray) axons until conduction block (motor = 13% of normal; sensory = 11% of normal). Note the logarithmic scaling of the *x*-axis.

that of conduction block, the more susceptible the myelinated axon becomes to the occurrence of a conduction block. As a result, additional, either internal or external, perturbations (e.g., membrane hyperpolarization or voluntary activity) that negatively affect the condition are likely to reduce this area or volume and may result in crossing of the slowing/block boundary, inducing failure of action potential propagation. Being close to this boundary is comparable to a reduced safety factor just above unity, where conduction is still possible, but slower. When it falls below unity by crossing the boundary, conduction failure eventually occurs (Franssen and Straver 2013, 2014). Interestingly, our findings further indicate that if conduction is still possible at the affected region, the membrane potential recovers outside such a region (Figs. 6*A* and 8*A*). This implies that multifocally affected regions within a myelinated axon do not necessarily lead to block, provided they are separated by sufficient distance. Nevertheless, as long as conduction is preserved, nerve function potentially varies depending on the distant from the affected region, which may explain the excitability studies in patients with MMN showing both abnormal (Garg et al. 2019) and normal excitability indexes outside the affected region (Cappelen-Smith et al. 2002). Further experimental evidence of this longitudinal recovery is also present in a study in which a rat myelinated fiber was partly exposed to anti-galactocerebroside serum and internodal conduction time normalized adjacent to the affected region (Lafontaine et al. 1982).

Simulating pathology. In various human neuropathies, the modeled pathology, including nodal sodium channel abnormalities and paranodal myelin loop detachment, was suggested to be of significant relevance. In CIDP, excitability changes in median nerve motor axons distal to sites with conduction block were consistent with increased current leakage between node and internode; furthermore, sera of these patients were shown to bind to nodal and paranodal regions of teased rat nerve fibers (Garg et al. 2019). In anti-MAG neuropathy, electron microscopy of sural nerve biopsy sections revealed loosening of paranodal Schwann cell microvilli (Kawagashira et al. 2010). Axonal excitability studies of median nerve motor axons showed decreased threshold changes during the supernormality period of the recovery cycle which were consistent with increased juxtaparanodal fast potassium channel activation due to loss of paranodal sealing (Garg et al. 2018). In diabetic neuropathy, latent addition revealed decreased nodal persistent sodium currents; this method allows for separation of changes in strength-duration properties due to passive nodal properties from those due to active nodal properties (Misawa et al. 2006). Axonal excitability studies in patients with type 1 diabetes without neuropathy showed changes consistent with loss of sodium permeability and decreased fast and slow potassium conductances (Kwai et al. 2016). Finally, staining of nodal sodium channels was shown to be decreased or lost in a rabbit model of human AMAN (Susuki et al. 2007b). Supporting our simulations, an experimental study showed that targeting sodium channels with lidocaine slows conduction, and therefore dysfunction of sodium channels should be considered as a mechanism of slowing, also in absence of block (Yokota et al. 1994). Similarly, exposure to anti-galactocerebroside antibodies was suggested to disrupt the outermost paranodal myelin loops from the paranodal axon, thus inducing slowing and block (Lafontaine et al. 1982). At a microstructural level, abnormalities in various proteins (Kieseier et al. 2018) may contribute to altered sodium channel conductance and paranodal seal resistance. GM1 gangliosides are enriched in the nodal and paranodal axolemma and maintain nodal sodium channel clustering and paranodal stabilization (Susuki et al. 2007b). Additionally, the septate-like junctions at the paranode are formed by axonal contactin-associated protein (Caspr1) and contactin 1 that are tightly connected to neurofascin-155 at the paranodal myelin loops. Nodal sodium channels are anchored to spectrin of the cytoskeleton via ankyrin-G and to gliomedin of the Schwann cell microvilli via neurofascin-186. As such, changes in functioning of these proteins may potentially be reflected within the model by dysfunction of sodium channels and detachment of paranodal myelin loops.

Sensitivity of the model to parameter choices. In addition to altering parameters to simulate pathology, it must be noted that small variations in any parameter within the model (e.g., dimensionality of the myelinated axon, ion channel conductances, gating kinetics, and longitudinal characteristics) will cause fluctuations in excitability properties, with levels of conduction slowing or block depending on the parameter's sensitivity within the model. Therefore, with the specific parameterization applied, the model structure, and simulation and stimulation settings, our findings should not be interpreted as rigid and absolute cutoff points regarding conduction slowing, conduction block, and varied response of the motor and sensory axons. More extensive and advanced probabilistic approaches are required to determine the contribution of these sources of variability (Mirams et al. 2016). Nevertheless, our simulation study provides a broad and quantitative insight into how single or interaction of multiple pathophysiological mechanisms may affect saltatory conduction, which otherwise cannot be systematically studied with experimental techniques.

Model limitations. The model includes the most prominent voltage-gated ion channels whose functioning has been experimentally studied in detail. Because completely capturing the

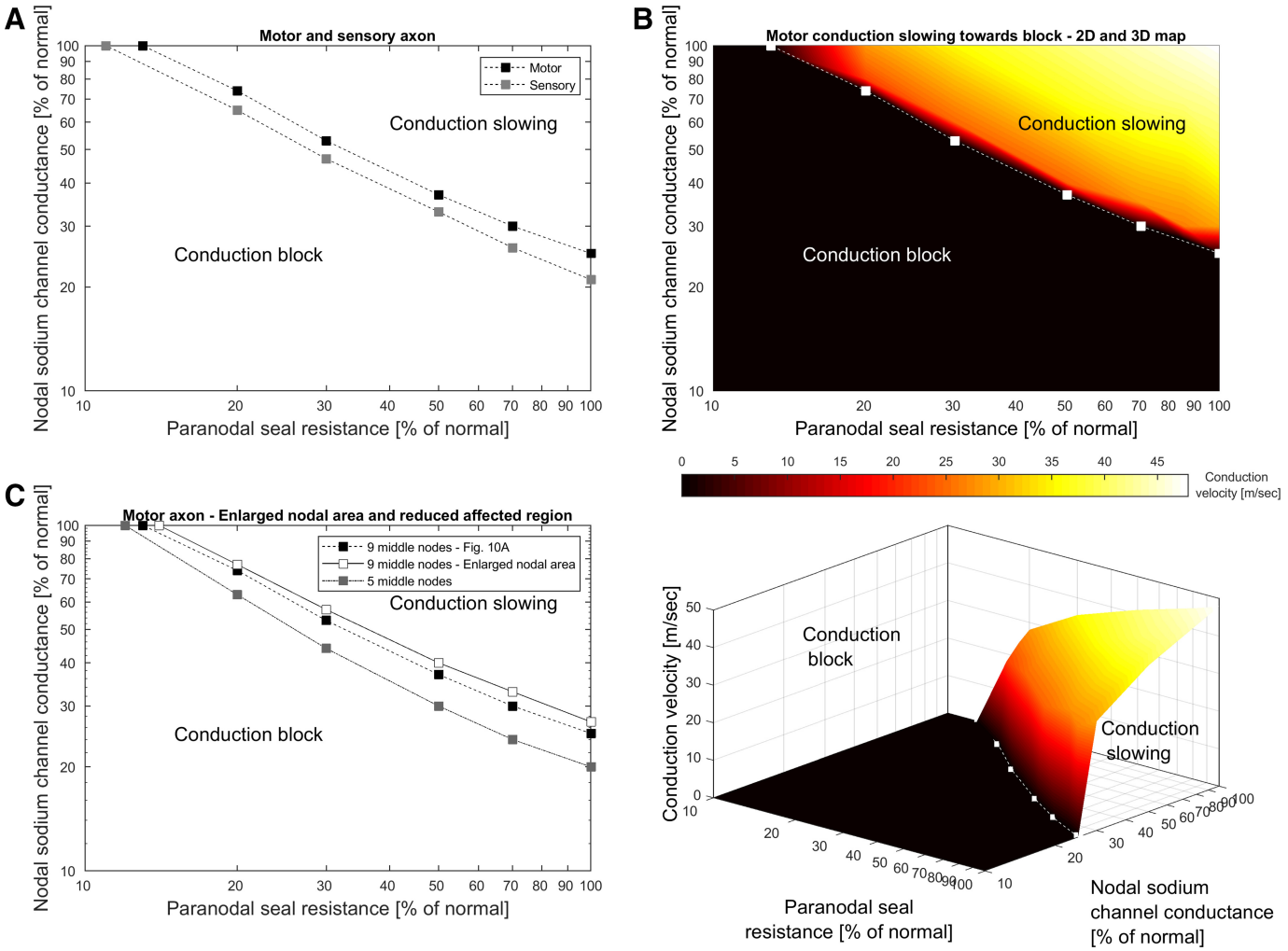

Fig. 10. Emergence of a boundary of block in motor and sensory axons due to the interaction of nodal sodium channel cluster disruption and paranodal myelin loop detachment, and effects of enlarged nodal area and a reduced affected region. *A*: the interaction of nodal sodium channel cluster disruption (as a percentage of normal nodal sodium channel conductance) and paranodal myelin loop detachment (as a percentage of normal paranodal seal resistance) in motor and sensory axon (9 middle nodes) for stimulation at 3 times the excitation threshold. *B*: 2-dimensional (*top*) and 3-dimensional (*bottom*) maps of motor conduction slowing toward block from interaction in *A*. *C*: boundary of block in motor axon in 9 middle nodes (closed squares, dashed line; same as *A*), 9 middle nodes with enlarged nodal area (open squares, solid line), and 5 middle nodes (shaded squares, dashed line). Note the logarithmic scaling of the axes.

functioning of a human peripheral myelinated axon in a computational model is impossible, these models always come with certain simplifications. It has also been suggested that ion channel types are present in the myelin membrane (Baker 2002; Chiu 1987). The myelin sheath in our model involved a myelin conductance and capacitance, which has also previously been applied (McIntyre et al. 2002; Stephanova and Bostock 1995), generating physiological conduction velocities and excitability properties. In addition to the gating kinetics, temperature also affects conductance, the electrogenic pump, and resting membrane potential (Franssen et al. 2010; Howells et al. 2013; Kovalchuk et al. 2018; Smit et al. 2009; Stephanova and Daskalova 2014). For convenience, we kept these parameters constant, because their values are less unambiguously defined to set properly. In the simulated temperature range (30–36°C), results matched experimental studies well, indicating the validity of our approach. The dynamics of extracellular and intracellular ion concentrations have not yet been incorporated into the model. The electrogenic pump represents a constant current, where more sophisticated models take into account its dependence on ion concentrations (Dijkstra et al. 2016). Repetitive nerve stimulation can result in potassium accumulation in the periaxonal space, which may also induce conduction block (Brazhe et al. 2011) or affect resting membrane potential and excitability of the nerve (Hageman et al. 2018). Because we restricted our study to simulations of action potential propagation after application of single stimuli, the expectation is that the above factors will have only a limited effect on our findings. Simulations of pathology were implemented homogenously in the affected region. When myelinated axons are pathologically targeted, they are likely to be affected more heterogeneously. Disturbed sodium channel clustering not only may be reflected by blockage of channel conductance but also potentially accompanies changes in gating kinetics. In pathological conditions, also implementing the expression of other sodium channel subtypes (e.g., Nav1.8) may become relevant to further refine the model, given there is some evidence of their presence in some nodes of Ranvier (Han et al. 2016). Because the membrane potential of the model is clamped, changes to conductances do not affect the

Table 3. *Ion channel gating variables with their corresponding equations*

Ion Channel Gating Variables	Equations
$\alpha_m, \alpha_p, \alpha_n, \alpha_s$	$\frac{A(V+B)}{1-e^{\frac{(-V-B)}{C}}}$
$\alpha_h, \beta_m, \beta_p, \beta_n, \beta_s$	$\frac{A(-V-B)}{1-e^{\frac{(V+B)}{C}}}$
β_h	$\frac{A}{1+e^{\frac{(-V-B)}{C}}}$
α_q	$Ae^{\frac{(-V-B)}{C}}$
β_q	$\frac{A}{e^{\frac{(-V-B)}{C}}}$

Variables m, h, p, s, n, and q are the dimensionless gates involving the transient sodium activation and inactivation, persistent sodium activation, slow and fast potassium activation, and hyperpolarization-activated nucleotide-gated cation activation, respectively. Rate constants (A), half-activation potentials (B), and slope factors (C) are presented in Table 4.

resting membrane potential. As such, the model allows study of changes to resting membrane potential as a separate mechanism. The above aspects can be further addressed in more detail in subsequent studies and provide interesting opportunities for improvements, depending on the research question posed.

Conclusion. With its current implementation, the presented model contains the most prominent biophysical aspects that appear necessary and sufficient to simulate saltatory conduction in motor and sensory axons. The link between these biophysical aspects and their varied impact on the emergence of block provides support that they may also partly contribute to the selective susceptibility in immune-mediated neuropathies. It further explains how action potential propagation becomes affected due to pathological mechanisms involved in immune-mediated neuropathies by focusing on perinodal changes. In various human neuropathies, such as anti-MAG neuropathy, these mechanisms may not remain restricted to the perinodal region but also may involve morphological changes associated with demyelination (Kawagashira et al. 2010). It therefore also provides a valuable platform that enables the implementation of, for example, segmental, paranodal, or juxtaparanodal demyelination (Franssen and Straver 2014; Stephanova et al. 2006, 2007) to further study their individual and composite impact on saltatory conduction. In CIDP and MMN, next to the morphological changes, also the interaction with increased or decreased currents through specific ion channels (e.g., juxtaparanodal fast potassium channels) is of clinical relevance to incorporate into the model (Garg et al. 2019). It may help to understand how these abnormalities can potentially be counteracted by specific pharmacological ion channel modifiers to prevent the occurrence of conduction block and restore action potential propagation. Computational models (Stephanova and Daskalova 2008), in conjunction with techniques to reliably assess the physiology and pathology in single human myelinated axons (Howells et al. 2018; Sleutjes et al. 2018), are valuable tools for providing insights into vital mechanisms that affect saltatory conduction and into which component may potentially be targeted in immune-mediated neuropathies.

APPENDIX

Below we present the basic equations in the model underlying the ionic currents, including their dynamics. For a more extensive description of the double-cable structure with the corresponding differential equations, we refer to the work of Danner et al. (2011b). The specific ionic currents, including their gating properties, were modeled according to the Hodgkin-Huxley formulation (Hodgkin and Huxley 1952). The transient and persistent sodium, slow and fast potassium, inward rectifying, and leak currents are described by

$$I_{\mathrm{Na_t}} = g_{\mathrm{Na_t}} m^3 h (V_{\mathrm{mem}} - E_{\mathrm{Na}}) \quad (A1)$$

$$I_{\mathrm{Na_p}} = g_{\mathrm{Na_p}} p^3 (V_{\mathrm{mem}} - E_{\mathrm{Na}}) \quad (A2)$$

$$I_{\mathrm{K_s}} = g_{\mathrm{K_s}} s (V_{\mathrm{mem}} - E_{\mathrm{K}}) \quad (A3)$$

$$I_{\mathrm{K_f}} = g_{\mathrm{K_f}} n^4 (V_{\mathrm{mem}} - E_{\mathrm{K}}) \quad (A4)$$

$$I_{\mathrm{H}} = g_{\mathrm{HCN}} q (V_{\mathrm{mem}} - E_{\mathrm{H}}) \quad (A5)$$

$$I_{\mathrm{L_k}} = g_{\mathrm{L_k}} (V_{\mathrm{mem}} - E_{\mathrm{L_k}}) \quad (A6)$$

Values for the conductances $g_{\mathrm{Na_t}}$, $g_{\mathrm{Na_p}}$, $g_{\mathrm{K_s}}$, $g_{\mathrm{K_f}}$, g_{HCN}, and $g_{\mathrm{L_k}}$ are given in Table 2. The variables m, h, p, s, n, and q are the dimensionless gates involving the transient sodium activation and inactivation, persistent sodium activation, slow and fast potassium activation,

Table 4. *Rate constants, half-activation potentials, and slope factors for motor and sensory axons*

	Rate Constant A, ms^{-1} (T_{ref} = 20°C)		Half-Activation Potential B, mV		Slope Factor C, mV	
Variable	Motor	Sensory[a]	Motor	Sensory[a,b]	Motor	Sensory[a]
α_m	1.86	1.778	20.4	20.2	10.3	
β_m	0.0861	0.0824	25.7	25.5	9.16	
α_p	0.01	0.0096	27.0	26.8	10.2	
β_p	0.00025	0.00024	34.0	33.8	10.0	
α_h	0.0619	0.075	113.8	112.5	11.0	8.4
β_h	2.294	2.800	31.8	30.5	13.4	10.2
α_n	0.008		83.2		1.1	
β_n	0.0142		66		10.5	
α_s	0.00097		23.5		12.7	
β_s	0.00059		91.1		11.7	
α_q, β_q	0.0009		107.3	101.0	12.2	

Values are rate constants (A), half-activation potentials (B), and slope factors (C) for gating variables m, h, p, s, n, and q in motor and sensory axons. [a]Changes of sensory-to-motor sodium channel activation gate (m, p) and inactivation gate (h), similar to those in Howells et al. (2012). [b]Depolarization of the half-activation of hyperpolarization-activated nucleotide-gated cation channels by 6.3 mV (see text).

and HCN activation, respectively. V_{mem} is the membrane potential. The ionic reversal potentials (Howells et al. 2012; Jankelowitz et al. 2007) are given by

$$E_{ion} = \frac{RT}{F}\log\left(\frac{[K]_{ex} + Sel_{ion}[Na]_{ex} - Sel_{ion}[K]_{ex}}{[K]_i + Sel_{ion}[Na]_i - Sel_{ion}[K]_i}\right), \quad (A7)$$

where E_{ion} represents the reversal potentials for sodium (E_{Na}), potassium (E_K), and inward rectifier (E_H). E_{L_k} is set to resting potential (V_{rest}). The applied channel selectivities Sel_{ion} were $Sel_{Na} = 0.9$, $Sel_K = 0$, and $Sel_H = 0.097$ (Howells et al. 2012). The applied intracellular ($[K]_i$, $[Na]_i$) and extracellular potassium and sodium concentrations ($[K]_{ex}$, $[Na]_{ex}$) were comparable to those in previous studies (Kiernan et al. 2005; Schwarz et al. 1995; Smit et al. 2009) with $[K]_{ex} = 5.6$ mM, $[K]_i = 155$ mM, $[Na]_i = 9$ mM, and $[Na]_{ex} = 144.2$ mM, and F and R are Faraday's constant, 96,485 C/mol and the gas constant, 8.315 J/mol K. The dynamics of the channel gates were described by

$$\frac{dy}{dt} = [\alpha_y(1 - y) - \beta_y y]Q_{10}^{\frac{T_{sim} - T_{ref}}{10}}, \quad (A8)$$

where y represents the channel gates (i.e., m, h, p, s, n, q), and α_y and β_y were derived using the equations shown in Table 3 and corresponding parameters shown in Table 4 (Howells et al. 2012; Jankelowitz et al. 2007; Kiernan et al. 2005; McIntyre et al. 2002).

The temperature dependencies are given by Q_{10} ($Q_{10} = 2.2$ for m and p gates, $Q_{10} = 2.9$ for h gate, and $Q_{10} = 3.0$ for n, s, and q gates). The default simulated temperature (T_{sim}) was 36°C, and the reference temperature (T_{ref}) was 20°C. At $t = 0$, the initial conditions for the gating kinetics satisfied (Hodgkin and Huxley 1952)

$$y_{t=0} = \frac{\alpha_y}{\alpha_y + \beta_y}, \quad (A9)$$

where $y_{t=0}$ represents the initial state of the gates. To ensure a net zero current at resting membrane potential across the axonal membrane in the compartments with voltage-gated ion channels, a small auxiliary current is implemented to initialize the model (Carnevale and Hines 2009).

GRANTS

This study was supported by the European Federation of Neurological Societies Scientific Fellowship and Prinses Beatrix Spierfonds Grant W.OR14-07.

DISCLOSURES

No conflicts of interest, financial or otherwise, are declared by the authors.

AUTHOR CONTRIBUTIONS

B.T.H.M.S., M.O.K., N.D., L.H.v.d.B., and H.F. conceived and designed research; B.T.H.M.S. and N.D. performed experiments; B.T.H.M.S., N.D., and H.F. analyzed data; B.T.H.M.S., M.O.K., N.D., J.R.B., M.J.A.M.v.P., L.H.v.d.B., and H.F. interpreted results of experiments; B.T.H.M.S., M.O.K., and H.F. prepared figures; B.T.H.M.S., M.O.K., L.H.v.d.B., and H.F. drafted manuscript; B.T.H.M.S., M.O.K., N.D., J.R.B., M.J.A.M.v.P., L.H.v.d.B., and H.F. edited and revised manuscript; B.T.H.M.S., M.O.K., N.D., J.R.B., M.J.A.M.v.P., L.H.v.d.B., and H.F. approved final version of manuscript.

REFERENCES

Baker M, Bostock H, Grafe P, Martius P. Function and distribution of three types of rectifying channel in rat spinal root myelinated axons. *J Physiol* 383: 45–67, 1987. doi:10.1113/jphysiol.1987.sp016395.

Baker MD. Electrophysiology of mammalian Schwann cells. *Prog Biophys Mol Biol* 78: 83–103, 2002. doi:10.1016/S0079-6107(02)00007-X.

Barrett EF, Barrett JN. Intracellular recording from vertebrate myelinated axons: mechanism of the depolarizing afterpotential. *J Physiol* 323: 117–144, 1982. doi:10.1113/jphysiol.1982.sp014064.

Berthold CH, Rydmark M. Morphology of normal peripheral axons. In: *The Axon*, edited by Waxman SG, Kocsis JD, Stys PK. New York: Oxford University Press, 1995, p. 13–48.

Blight AR. Computer simulation of action potentials and afterpotentials in mammalian myelinated axons: the case for a lower resistance myelin sheath. *Neuroscience* 15: 13–31, 1985. doi:10.1016/0306-4522(85)90119-8.

Bostock H. The strength-duration relationship for excitation of myelinated nerve: computed dependence on membrane parameters. *J Physiol* 341: 59–74, 1983. doi:10.1113/jphysiol.1983.sp014792.

Bostock H, Burke D, Hales JP. Differences in behaviour of sensory and motor axons following release of ischaemia. *Brain* 117: 225–234, 1994. doi:10.1093/brain/117.2.225.

Bostock H, Rothwell JC. Latent addition in motor and sensory fibres of human peripheral nerve. *J Physiol* 498: 277–294, 1997. doi:10.1113/jphysiol.1997.sp021857.

Boyd IA, Kalu KU. Scaling factor relating conduction velocity and diameter for myelinated afferent nerve fibres in the cat hind limb. *J Physiol* 289: 277–297, 1979. doi:10.1113/jphysiol.1979.sp012737.

Brazhe AR, Maksimov GV, Mosekilde E, Sosnovtseva OV. Excitation block in a nerve fibre model owing to potassium-dependent changes in myelin resistance. *Interface Focus* 1: 86–100, 2011. doi:10.1098/rsfs.2010.0001.

Burke D, Howells J, Kiernan MC. Sensory and motor axons are different: implications for neurological disease. *Ann Clin Neurophysiol* 19: 3–12, 2017. doi:10.14253/acn.2017.19.1.3

Burke D, Kiernan M, Mogyoros I, Bostock H. Susceptibility to conduction block - differences in the biophysical properties of cutaneous afferents and motor axons. In: *Physiology of ALS and Related Diseases*, edited by Kimura J, Kaji R. Amsterdam: Elsevier, 1997, p. 43–53.

Burke D, Kiernan MC, Bostock H. Excitability of human axons. *Clin Neurophysiol* 112: 1575–1585, 2001. doi:10.1016/S1388-2457(01)00595-8.

Cappelen-Smith C, Kuwabara S, Lin CS, Burke D. Abnormalities of axonal excitability are not generalized in early multifocal motor neuropathy. *Muscle Nerve* 26: 769–776, 2002. doi:10.1002/mus.10262.

Carnevale NT, Hines ML. *The NEURON Book*. New York: Cambridge University Press, 2009, p. 480.

Chiu SY. Sodium currents in axon-associated Schwann cells from adult rabbits. *J Physiol* 386: 181–203, 1987. doi:10.1113/jphysiol.1987.sp016529.

Danner SM, Hofstoetter US, Ladenbauer J, Rattay F, Minassian K. Can the human lumbar posterior columns be stimulated by transcutaneous spinal cord stimulation? A modeling study. *Artif Organs* 35: 257–262, 2011a. doi:10.1111/j.1525-1594.2011.01213.x.

Danner SM, Wenger C, Rattay F. *Electrical Stimulation of Myelinated Axons—An Interactive Tutorial Supported by Computer Simulation*. Saarbrücken, Germany: VDM Verlag Dr Müller, 2011b.

Daskalova M, Stephanova DI. Strength-duration properties of human myelinated motor and sensory axons in normal case and in amyotrophic lateral sclerosis. *Acta Physiol Pharmacol Bulg* 26: 11–14, 2001.

Davis FA, Schauf CL, Reed BJ, Kesler RL. Experimental studies of the effects of extrinsic factors on conduction in normal and demyelinated nerve. 1. Temperature. *J Neurol Neurosurg Psychiatry* 39: 442–448, 1976. doi:10.1136/jnnp.39.5.442.

de Jesus PV, Hausmanowa-Petrusewicz I, Barchi RL. The effect of cold on nerve conduction of human slow and fast nerve fibers. *Neurology* 23: 1182–1189, 1973. doi:10.1212/WNL.23.11.1182.

Delmont E, Manso C, Querol L, Cortese A, Berardinelli A, Lozza A, Belghazi M, Malissart P, Labauge P, Taieb G, Yuki N, Illa I, Attarian S, Devaux JJ. Autoantibodies to nodal isoforms of neurofascin in chronic inflammatory demyelinating polyneuropathy. *Brain* 140: 1851–1858, 2017. doi:10.1093/brain/awx124.

Devaux JJ, Miura Y, Fukami Y, Inoue T, Manso C, Belghazi M, Sekiguchi K, Kokubun N, Ichikawa H, Wong AH, Yuki N. Neurofascin-155 IgG4 in chronic inflammatory demyelinating polyneuropathy. *Neurology* 86: 800–807, 2016. doi:10.1212/WNL.0000000000002418.

Dijkstra K, Hofmeijer J, van Gils SA, van Putten MJ. A biophysical model for cytotoxic cell swelling. *J Neurosci* 36: 11881–11890, 2016. doi:10.1523/JNEUROSCI.1934-16.2016.

Fitzhugh R. Computation of impulse initiation and saltatory conduction in a myelinated nerve fiber. *Biophys J* 2: 11–21, 1962. doi:10.1016/S0006-3495(62)86837-4.

Franssen H. Relation between symptoms and pathophysiology in inflammatory neuropathies: controversies and hypotheses. *Neurosci Lett* 596: 84–89, 2015. doi:10.1016/j.neulet.2014.12.009.

Franssen H, Gebbink TA, Wokke JH, van den Berg LH, van Schelven LJ. Is cold paresis related to axonal depolarization? *J Peripher Nerv Syst* 15: 227–237, 2010. doi:10.1111/j.1529-8027.2010.00275.x.

Franssen H, Straver DC. Pathophysiology of immune-mediated demyelinating neuropathies–Part I: Neuroscience. *Muscle Nerve* 48: 851–864, 2013. doi:10.1002/mus.24070.

Franssen H, Straver DC. Pathophysiology of immune-mediated demyelinating neuropathies–Part II: Neurology. *Muscle Nerve* 49: 4–20, 2014. doi:10.1002/mus.24068.

Franssen H, Wieneke GH. Nerve conduction and temperature: necessary warming time. *Muscle Nerve* 17: 336–344, 1994. doi:10.1002/mus.880170313.

Garg N, Park SB, Howells J, Noto YI, Vucic S, Yiannikas C, Tomlinson SE, Huynh W, Simon NG, Mathey EK, Spies J, Pollard JD, Krishnan AV, Kiernan MC. Anti-MAG neuropathy: role of IgM antibodies, the paranodal junction and juxtaparanodal potassium channels. *Clin Neurophysiol* 129: 2162–2169, 2018. doi:10.1016/j.clinph.2018.07.021.

Garg N, Park SB, Howells J, Vucic S, Yiannikas C, Mathey EK, Nguyen T, Noto Y, Barnett MH, Krishnan AV, Spies J, Bostock H, Pollard JD, Kiernan MC. Conduction block in immune-mediated neuropathy: paranodopathy versus axonopathy. *Eur J Neurol* 26: 1121–1129, 2019. doi:10.1111/ene.13953.

Goldman L, Albus JS. Computation of impulse conduction in myelinated fibers; theoretical basis of the velocity-diameter relation. *Biophys J* 8: 596–607, 1968. doi:10.1016/S0006-3495(68)86510-5.

Hageman S, Kovalchuk MO, Sleutjes BT, van Schelven LJ, van den Berg LH, Franssen H. Sodium-potassium pump assessment by submaximal electrical nerve stimulation. *Clin Neurophysiol* 129: 809–814, 2018. doi:10.1016/j.clinph.2018.01.016.

Halar EM, DeLisa JA, Brozovich FV. Nerve conduction velocity: relationship of skin, subcutaneous and intramuscular temperatures. *Arch Phys Med Rehabil* 61: 199–203, 1980.

Hales JP, Lin CS, Bostock H. Variations in excitability of single human motor axons, related to stochastic properties of nodal sodium channels. *J Physiol* 559: 953–964, 2004. doi:10.1113/jphysiol.2004.068726.

Halter JA, Clark JW Jr. A distributed-parameter model of the myelinated nerve fiber. *J Theor Biol* 148: 345–382, 1991. doi:10.1016/S0022-5193(05)80242-5.

Han C, Huang J, Waxman SG. Sodium channel Nav1.8: emerging links to human disease. *Neurology* 86: 473–483, 2016. doi:10.1212/WNL.0000000000002333.

Hennings K, Arendt-Nielsen L, Andersen OK. Breakdown of accommodation in nerve: a possible role for persistent sodium current. *Theor Biol Med Model* 2: 16, 2005. doi:10.1186/1742-4682-2-16.

Hindmarsh AC, Brown PN, Grant KE, Lee SL, Serban R, Shumaker DE, Woodward CS. SUNDIALS: suite of nonlinear and differential/algebraic equation solvers. *ACM Trans Math Softw* 31: 363–396, 2005. doi:10.1145/1089014.1089020

Hodgkin AL, Huxley AF. A quantitative description of membrane current and its application to conduction and excitation in nerve. *J Physiol* 117: 500–544, 1952. doi:10.1113/jphysiol.1952.sp004764.

Honmou O, Utzschneider DA, Rizzo MA, Bowe CM, Waxman SG, Kocsis JD. Delayed depolarization and slow sodium currents in cutaneous afferents. *J Neurophysiol* 71: 1627–1637, 1994. doi:10.1152/jn.1994.71.5.1627.

Howells J, Czesnik D, Trevillion L, Burke D. Excitability and the safety margin in human axons during hyperthermia. *J Physiol* 591: 3063–3080, 2013. doi:10.1113/jphysiol.2012.249060.

Howells J, Matamala JM, Park SB, Garg N, Vucic S, Bostock H, Burke D, Kiernan MC. In vivo evidence for reduced ion channel expression in motor axons of patients with amyotrophic lateral sclerosis. *J Physiol* 596: 5379–5396, 2018. doi:10.1113/JP276624.

Howells J, Trevillion L, Bostock H, Burke D. The voltage dependence of I_h in human myelinated axons. *J Physiol* 590: 1625–1640, 2012. doi:10.1113/jphysiol.2011.225573.

Jankelowitz SK, Howells J, Burke D. Plasticity of inwardly rectifying conductances following a corticospinal lesion in human subjects. *J Physiol* 581: 927–940, 2007. doi:10.1113/jphysiol.2006.123661.

Kaji R. Physiology of conduction block in multifocal motor neuropathy and other demyelinating neuropathies. *Muscle Nerve* 27: 285–296, 2003. doi:10.1002/mus.10273.

Kawagashira Y, Koike H, Tomita M, Morozumi S, Iijima M, Nakamura T, Katsuno M, Tanaka F, Sobue G. Morphological progression of myelin abnormalities in IgM-monoclonal gammopathy of undetermined significance anti-myelin-associated glycoprotein neuropathy. *J Neuropathol Exp Neurol* 69: 1143–1157, 2010. doi:10.1097/NEN.0b013e3181fa44af.

Kiernan MC, Burke D, Andersen KV, Bostock H. Multiple measures of axonal excitability: a new approach in clinical testing. *Muscle Nerve* 23: 399–409, 2000. doi:10.1002/(SICI)1097-4598(200003)23:3<399:AID-MUS12>3.0.CO;2-G.

Kiernan MC, Isbister GK, Lin CS, Burke D, Bostock H. Acute tetrodotoxin-induced neurotoxicity after ingestion of puffer fish. *Ann Neurol* 57: 339–348, 2005. doi:10.1002/ana.20395.

Kiernan MC, Lin CS, Andersen KV, Murray NM, Bostock H. Clinical evaluation of excitability measures in sensory nerve. *Muscle Nerve* 24: 883–892, 2001. doi:10.1002/mus.1085.

Kiernan MC, Lin CS, Burke D. Differences in activity-dependent hyperpolarization in human sensory and motor axons. *J Physiol* 558: 341–349, 2004. doi:10.1113/jphysiol.2004.063966.

Kieseier BC, Mathey EK, Sommer C, Hartung HP. Immune-mediated neuropathies. *Nat Rev Dis Primers* 4: 31, 2018. doi:10.1038/s41572-018-0027-2.

Kleinberg CS, Arroyo EJ, King C, Scherer SS. Na,K-ATPase isoforms in the PNS: cell-type specific expression and internodal localization in myelinated axons (Abstract). *J Peripher Nerv Syst* 12, *Suppl*: 45, 2007.

Kocsis JD, Eng DL, Gordon TR, Waxman SG. Functional differences between 4-aminopyridine and tetraethylammonium-sensitive potassium channels in myelinated axons. *Neurosci Lett* 75: 193–198, 1987. doi:10.1016/0304-3940(87)90296-5.

Koles ZJ, Rasminsky M. A computer simulation of conduction in demyelinated nerve fibres. *J Physiol* 227: 351–364, 1972. doi:10.1113/jphysiol.1972.sp010036.

Kovalchuk MO, Franssen H, Van Schelven LJ, Sleutjes BT. Comparing excitability at 37°C versus at 20°C: differences between motor and sensory axons. *Muscle Nerve* 57: 574–580, 2018. doi:10.1002/mus.25960.

Krouchev NI, Danner SM, Vinet A, Rattay F, Sawan M. Energy-optimal electrical-stimulation pulses shaped by the least-action principle. *PLoS One* 9: e90480, 2014. doi:10.1371/journal.pone.0090480.

Kuhn A, Keller T, Lawrence M, Morari M. A model for transcutaneous current stimulation: simulations and experiments. *Med Biol Eng Comput* 47: 279–289, 2009. doi:10.1007/s11517-008-0422-z.

Kwai NCG, Arnold R, Poynten AM, Howells J, Kiernan MC, Lin CS, Krishnan AV. In vivo evidence of reduced nodal and paranodal conductances in type 1 diabetes. *Clin Neurophysiol* 127: 1700–1706, 2016. doi:10.1016/j.clinph.2015.11.047.

Lafontaine S, Rasminsky M, Saida T, Sumner AJ. Conduction block in rat myelinated fibres following acute exposure to anti-galactocerebroside serum. *J Physiol* 323: 287–306, 1982. doi:10.1113/jphysiol.1982.sp014073.

Lowitzsch K, Hopf HC, Galland J. Changes of sensory conduction velocity and refractory periods with decreasing tissue temperature in man. *J Neurol* 216: 181–188, 1977. doi:10.1007/BF00313619.

McIntyre CC, Richardson AG, Grill WM. Modeling the excitability of mammalian nerve fibers: influence of afterpotentials on the recovery cycle. *J Neurophysiol* 87: 995–1006, 2002. doi:10.1152/jn.00353.2001.

Mirams GR, Pathmanathan P, Gray RA, Challenor P, Clayton RH. Uncertainty and variability in computational and mathematical models of cardiac physiology. *J Physiol* 594: 6833–6847, 2016. doi:10.1113/JP271671.

Misawa S, Kuwabara S, Kanai K, Tamura N, Nakata M, Ogawara K, Yagui K, Hattori T. Nodal persistent Na^+ currents in human diabetic nerves estimated by the technique of latent addition. *Clin Neurophysiol* 117: 815–820, 2006. doi:10.1016/j.clinph.2005.11.019.

Mitrović N, Quasthoff S, Grafe P. Sodium channel inactivation kinetics of rat sensory and motor nerve fibres and their modulation by glutathione. *Pflugers Arch* 425: 453–461, 1993. doi:10.1007/BF00374872.

Mogyoros I, Kiernan MC, Burke D. Strength-duration properties of human peripheral nerve. *Brain* 119: 439–447, 1996. doi:10.1093/brain/119.2.439.

Mogyoros I, Kiernan MC, Burke D, Bostock H. Excitability changes in human sensory and motor axons during hyperventilation and ischaemia. *Brain* 120: 317–325, 1997. doi:10.1093/brain/120.2.317.

Moore JW, Joyner RW, Brill MH, Waxman SD, Najar-Joa M. Simulations of conduction in uniform myelinated fibers. Relative sensitivity to changes in nodal and internodal parameters. *Biophys J* 21: 147–160, 1978. doi:10.1016/S0006-3495(78)85515-5.

Nielsen VK. Sensory and motor nerve conduction in the median nerve in normal subjects. *Acta Med Scand* 194: 435–443, 1973. doi:10.1111/j.0954-6820.1973.tb19469.x.

Paintal AS. Block of conduction in mammalian myelinated nerve fibres by low temperatures. *J Physiol* 180: 1–19, 1965.

Rasminsky M. The effects of temperature on conduction in demyelinated single nerve fibers. *Arch Neurol* 28: 287–292, 1973. doi:10.1001/archneur.1973.00490230023001.

Ritchie JM. Physiology of axons. In: *The Axon*, edited by Waxman SG, Kocsis JD, Stys PK. New York: Oxford University Press, 1995, p. 68–96.

Schwarz JR, Bromm B, Spielmann RP, Weytjens JL. Development of Na inactivation in motor and sensory myelinated nerve fibres of *Rana esculenta*. *Pflugers Arch* 398: 126–129, 1983. doi:10.1007/BF00581059.

Schwarz JR, Eikhof G. Na currents and action potentials in rat myelinated nerve fibres at 20 and 37°C. *Pflugers Arch* 409: 569–577, 1987. doi:10.1007/BF00584655.

Schwarz JR, Reid G, Bostock H. Action potentials and membrane currents in the human node of Ranvier. *Pflugers Arch* 430: 283–292, 1995. doi:10.1007/BF00374660.

Sleutjes BT, Drenthen J, Boskovic E, van Schelven LJ, Kovalchuk MO, Lumens PG, van den Berg LH, Franssen H. Excitability tests using high-density surface-EMG: a novel approach to studying single motor units. *Clin Neurophysiol* 129: 1634–1641, 2018. doi:10.1016/j.clinph.2018.04.754.

Smit JE, Hanekom T, Hanekom JJ. Modelled temperature-dependent excitability behaviour of a generalised human peripheral sensory nerve fibre. *Biol Cybern* 101: 115–130, 2009. doi:10.1007/s00422-009-0324-7.

Stephanova DI, Alexandrov AS, Kossev A, Christova L. Simulating focal demyelinating neuropathies: membrane property abnormalities. *Biol Cybern* 96: 195–208, 2007. doi:10.1007/s00422-006-0113-5.

Stephanova DI, Bostock H. A distributed-parameter model of the myelinated human motor nerve fibre: temporal and spatial distributions of action potentials and ionic currents. *Biol Cybern* 73: 275–280, 1995. doi:10.1007/BF00201429.

Stephanova DI, Daskalova M. Effects of temperature on simulated electrotonic potentials and their current kinetics of human motor axons at 20°C–42°C. *J Integr Neurosci* 13: 447–464, 2014. doi:10.1142/S0219635214500095.

Stephanova DI, Daskalova MS. Differences between the channels, currents and mechanisms of conduction slowing/block and accommodative processes in simulated cases of focal demyelinating neuropathies. *Eur Biophys J* 37: 829–842, 2008. doi:10.1007/s00249-008-0284-1.

Stephanova DI, Daskalova MS, Alexandrov AS. Differences in membrane properties in simulated cases of demyelinating neuropathies: internodal focal demyelinations without conduction block. *J Biol Phys* 32: 61–71, 2006. doi:10.1007/s10867-005-9001-9.

Susuki K. Node of Ranvier disruption as a cause of neurological diseases. *ASN Neuro* 5: 209–219, 2013. doi:10.1042/AN20130025.

Susuki K, Baba H, Tohyama K, Kanai K, Kuwabara S, Hirata K, Furukawa K, Furukawa K, Rasband MN, Yuki N. Gangliosides contribute to stability of paranodal junctions and ion channel clusters in myelinated nerve fibers. *Glia* 55: 746–757, 2007a. doi:10.1002/glia.20503.

Susuki K, Rasband MN, Tohyama K, Koibuchi K, Okamoto S, Funakoshi K, Hirata K, Baba H, Yuki N. Anti-GM1 antibodies cause complement-mediated disruption of sodium channel clusters in peripheral motor nerve fibers. *J Neurosci* 27: 3956–3967, 2007b. doi:10.1523/JNEUROSCI.4401-06.2007.

Susuki K, Yuki N, Schafer DP, Hirata K, Zhang G, Funakoshi K, Rasband MN. Dysfunction of nodes of Ranvier: a mechanism for anti-ganglioside antibody-mediated neuropathies. *Exp Neurol* 233: 534–542, 2012. doi:10.1016/j.expneurol.2011.11.039.

Tasaki I. *Nervous Transmission*. Springfield, IL: Thomas, 1953.

Uncini A, Kuwabara S. Nodopathies of the peripheral nerve: an emerging concept. *J Neurol Neurosurg Psychiatry* 86: 1186–1195, 2015. doi:10.1136/jnnp-2014-310097.

Waxman SG, Kocsis JD, Stys PK. *The Axon*. New York: Oxford University Press, 1995.

Waxman SG, Ritchie JM. Molecular dissection of the myelinated axon. *Ann Neurol* 33: 121–136, 1993. doi:10.1002/ana.410330202.

Yokota T, Saito Y, Miyatake T. Conduction slowing without conduction block of compound muscle and nerve action potentials due to sodium channel block. *J Neurol Sci* 124: 220–224, 1994. doi:10.1016/0022-510X(94)90330-1.

Yuki N, Yamada M, Koga M, Odaka M, Susuki K, Tagawa Y, Ueda S, Kasama T, Ohnishi A, Hayashi S, Takahashi H, Kamijo M, Hirata K. Animal model of axonal Guillain-Barré syndrome induced by sensitization with GM1 ganglioside. *Ann Neurol* 49: 712–720, 2001. doi:10.1002/ana.1012.